Check for updates

Enhancing the photocatalytic activity of Cu$_{0.25}$Zn$_{0.75}$S nanodisks by metallic Ag loading in the visible-light region

Jinyang Zhang, [ID] [a] Fuyan Kang,[a] Hao Peng, [ID] *[b] Jing Wen [ID] *[c] and Xiaogang Zheng[a]

Ag-loaded Cu$_{0.25}$Zn$_{0.75}$S (Ag/Cu$_{0.25}$Zn$_{0.75}$S) photocatalysts were synthesized for the photodegradation of organic pollutants such as rhodamine B (RhB), methyl violet (MV) and ciprofloxacin hydrochloride (CIP) under visible-light irradiation. Metallic Ag facilitated the enhancement of the photocatalytic activity of Cu$_{0.25}$Zn$_{0.75}$S nanodisks, and a Ag loading content of 11% exhibited great degradation efficiency for the degradation of RhB with the assistance of H$_2$O$_2$ under acidic conditions. This sample presented slight deactivation for the visible-light-driven degradation of RhB after five cycles. In addition, the excellent photocatalytic activity of Ag/Cu$_{0.25}$Zn$_{0.75}$S was obtained for the removal of MV and CIP. $\cdot$O$_2^-$ is mainly responsible for the efficient activity of the photocatalytic process.

1. Introduction

Transition metal sulfides have attracted extensive attention in solar energy utilization and environmental protection.[1–8] Among the transition metal sulfide semiconductors, ZnS and CuS are considered to be promising photocatalysts due to their low cost and nonexistent secondary pollution.[4,9,10] Some studies have shown that the combination of ZnS with a wide band gap (3.72 eV for the cubic phase and 3.77 eV for the hexagonal phase) and CuS with a narrow band gap (2.2 eV) can make up for the defects of a single compound and significantly enhance photoelectric response performance and the visible-light photocatalytic activity.[2,11–13] Pouretedal *et al.* reported that the visible-light-driven photoactivity of Zn$_{1-x}$Cu$_x$S (Zn$_{0.90}$Cu$_{0.10}$S) nanocomposites was higher than that of Zn$_{1-x}$Ni$_x$S (Zn$_{0.94}$Ni$_{0.06}$S) nanocomposites.[14] ZnS/CuS composites with a ZnS core and CuS shell prepared by the ion-exchange route exhibited inferior durability due to photocorrosion.[5,15,16] A CuS/ZnS core/shell structure was developed to passivate the trap states of CuS and restrain the photocorrosion, which can efficiently decompose methylene blue and rhodamine B under visible-light irradiation.[4,17,18] CuS–ZnS-based materials such as Cu$_x$Zn$_y$S films were prepared by pulsed laser deposition,[19] spray pyrolysis,[20] electrochemical deposition and photochemical deposition[12,21–25] to enhance the visible-light photocatalytic capacity. Besides, Cu–Zn–S-sensitized TiO$_2$ nanotube arrays (Cu–Zn–S/TiO$_2$ NTAs) exhibited excellent photocatalytic activity compared with TiO$_2$ NTAs.[12]

However, the wide band gap of Cu$_x$Zn$_y$S has been confirmed by some studies.[24,26,27] The band gap can be tuned by elemental doping. Doping can facilitate the transmission of photo-generated electrons and prevent the photocorrosion of the ZnS–CuS composites. Shifu C. *et al.* prepared Ce$_2$S$_3$–ZnS–CuS by the ball milling method and found that the photocatalytic activity of Ce$_2$S$_3$–ZnS–CuS was much higher than that of ZnS–CuS.[28] In addition, noble metals (such as Ag, Pt, Au) were frequently used as electron traps to promote the interfacial electron transfer processes.[29–31] Among them, Ag was the most suitable in industrial applications for its high efficiency, low cost and corrosion resistance. The doping of Ag at an optimum amount can improve the photocatalytic activity of ZnS by increasing visible light absorption and enhancing the charge separation by trapping electrons.[32–34] In addition to the doping, the loading of noble metals also showed better photocatalytic efficiency, such as in the Pt–BiOI nanoplates,[29] Ag/Au-doped CeO$_2$ nanoparticles,[35] and AgAg$_2$S–TiO$_2$ nanocomposites.[36]

In our recent study, Cu$_x$Zn$_{1-x}$S nanodisks were prepared by a hydrothermal method and presented the enhanced photocatalytic activity of RhB compared with those of pure ZnS and CuS.[37] Though Cu$_x$Zn$_{1-x}$S nanodisks had a narrow band gap, the catalytic activity and durability were affected by photocorrosion during the cycle testing process. Therefore, Ag/Cu$_x$Zn$_{1-x}$S composites were further designed to improve photocatalytic efficiency and stability. Different amounts of Ag were deposited on the surface of the Cu$_{0.25}$Zn$_{0.75}$S nanodisks by a photocatalytic deposition method, and the photocatalytic performance of the as-obtained Ag/Cu$_{0.25}$Zn$_{0.75}$S for the

[a] College of Chemistry and Chemical Engineering, Neijiang Normal University, Neijiang, Sichuan 641100, China

[b] College of Chemistry and Chemical Engineering, Yangtze Normal University, Chongqing 408100, China. E-mail: cqpenghao@126.com; Fax: +86 023 72792170; +86 0971 7762180; Tel: +86 023 72792170; +86 0971 7762180

[c] Key Laboratory of Comprehensive and Highly Efficient Utilization of Salt Lake Resources, Key Laboratory of Salt Lake Resources Chemistry of Qinghai Province, Qinghai Institute of Salt Lakes, Chinese Academy of Sciences, Xining, Qinghai 810008, China. E-mail: wj580420@163.com
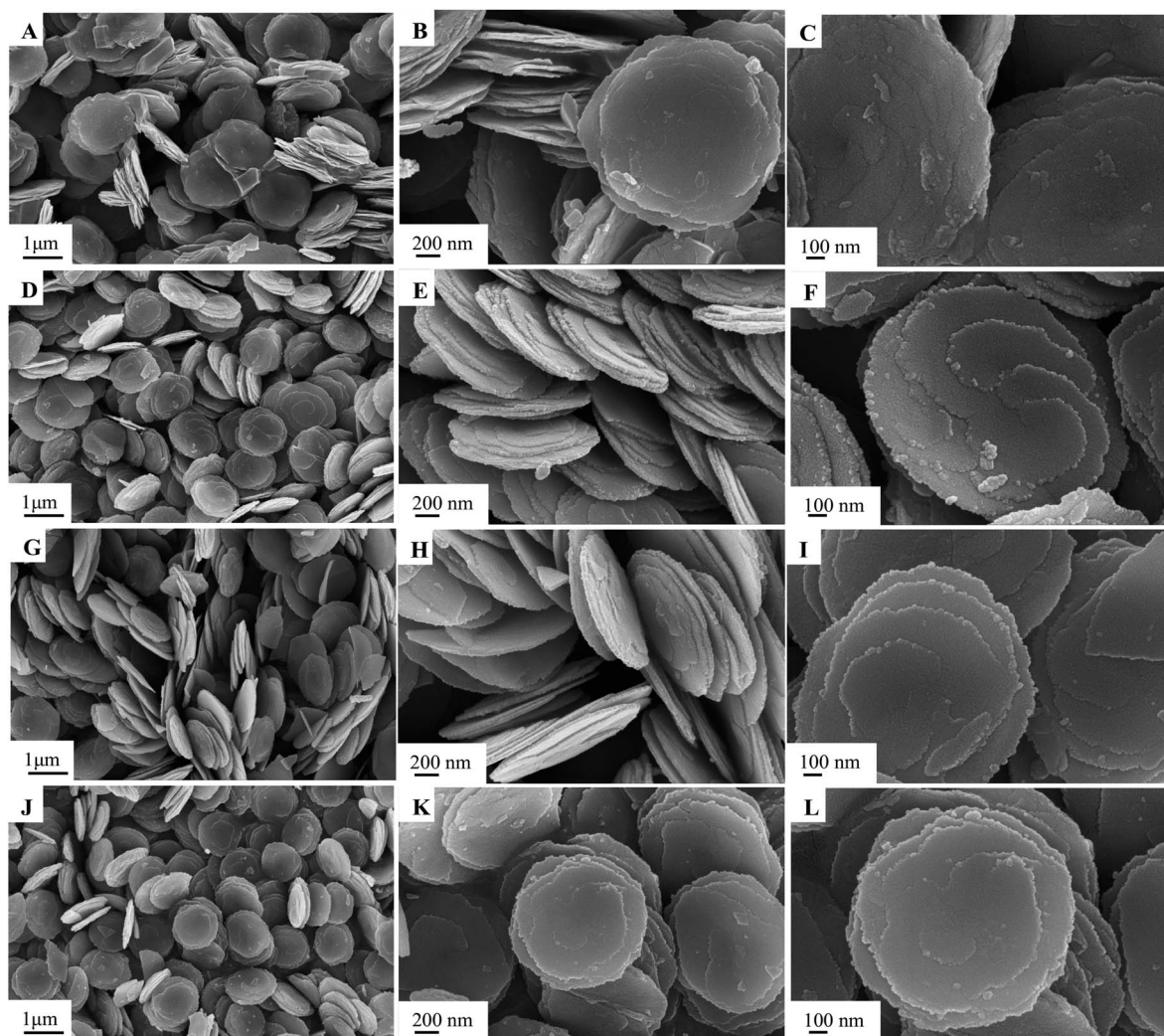
Fig. 1 SEM images of $Cu_{0.25}Zn_{0.75}S$ samples prepared at different temperatures: 140 °C (A–C), 160 °C (D–F), 180 °C (G–I), 200 °C (J–L).

degradation of organic contaminants was investigated under visible-light irradiation.

2. Experimental section

2.1 Synthesis of the $Cu_{0.25}Zn_{0.75}S$ nanodisk

The $Cu_{0.25}Zn_{0.75}S$ nanodisk was synthesized by a one-step hydrothermal method, as described in our previous work.[37] In a typical procedure, the total mass of $Cu(NO_3)_2 \cdot 3H_2O$ and $Zn(NO_3)_2 \cdot 6H_2O$ of 2, 4, 6 and 8 mmol with a Cu/Zn molar ratio of 1 : 3, 15 mmol of thiourea and 1 g of PVP were dissolved in 160 mL acetonitrile solution (50% v/v) and stirred at room temperature for 2 h. The resultant solution was transferred into a 200 mL Teflon-lined autoclave, which was then maintained at different temperatures (140–200 °C) for different time periods (3–12 h) and was left to cool to room temperature. The product was directly centrifuged and the resulting supernatant was discarded. The product was washed with water and ethanol three times and vacuum-dried at 50 °C for 10 h, providing the sample in the powder form. The effects of the total mass of cupric nitrate and zinc nitrate, the reaction temperature and the

reaction time on the structure of the $Cu_{0.25}Zn_{0.75}S$ nanodisk were investigated.

2.2 Synthesis of the $Ag/Cu_{0.25}Zn_{0.75}S$ catalyst

$Ag/Cu_{0.25}Zn_{0.75}S$ was prepared by a photocatalytic deposition method.[29] Brief descriptions are as follows. 0.1 g of $Cu_{0.25}Zn_{0.75}S$ was dispersed in different concentrations of $AgNO_3$ solution (the mass of Ag was 5%, 7%, 9%, 11% and 13% of $Cu_{0.25}Zn_{0.75}S$) by a sonicator and stirred at room temperature for 1 h. The resultant solution was irradiated by a 300 W metal halide lamp for 9 hours. The product was centrifuged and washed with water and ethanol three times. Finally, the sample was vacuum-dried at 50 °C for 10 h. These obtained samples were defined as 5-Ag/ $Cu_{0.25}Zn_{0.75}S$, 7-Ag/$Cu_{0.25}Zn_{0.75}S$, 9-Ag/$Cu_{0.25}Zn_{0.75}S$, 11-Ag/ $Cu_{0.25}Zn_{0.75}S$, and 13-Ag/$Cu_{0.25}Zn_{0.75}S$.

2.3 Characterization of the catalysts

Scanning electron microscopy (SEM) images were obtained using a JSM-5610LV/INCA scanning electron microscope operating at 20 kV. Powder X-ray diffraction (XRD) patterns were
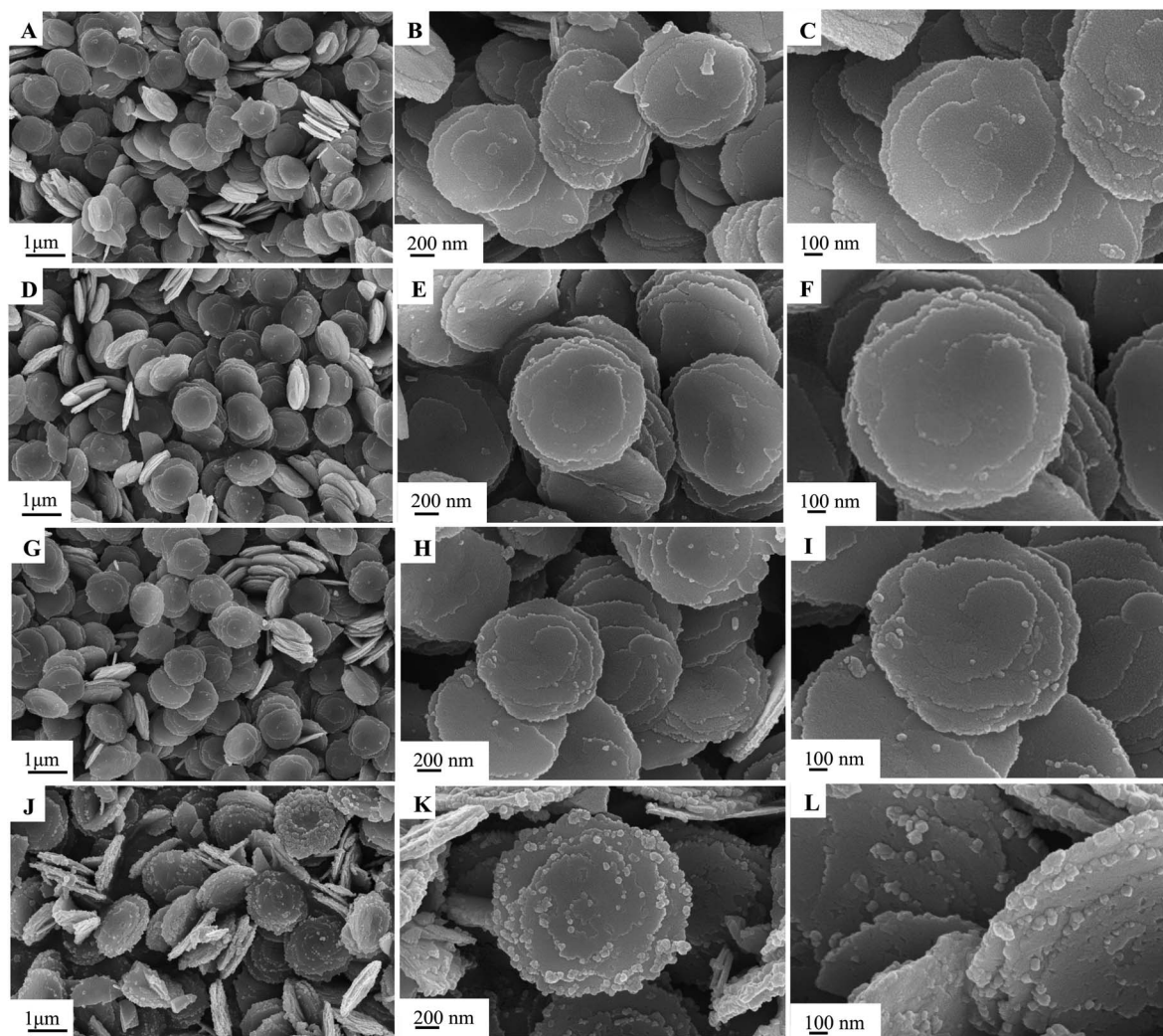
Fig. 2 SEM images of $Cu_{0.25}Zn_{0.75}S$ prepared with varying reaction times of 3 h (A–C), 6 h (D–F), 8 h (G–I), 12 h (J–L).

conducted with a Shimadzu LabX XRD-6000 X-ray diffractometer with Cu K_{α} radiation (1.54 Å) and a scanning speed of 5° min^{-1}. The accelerating voltage and emission current were 40 kV and 100 mA, respectively. X-ray photoelectron spectra (XPS) were recorded by using an ESCALAB 250Xi (Thermo Fisher) with an operating voltage of 15 kV and a spot size of 400 μm. The Brunauer–Emmett–Teller (BET) specific surface areas were carried out using a Quantachrome NOVA-2020 analyzer. UV-vis diffuse reflectance spectra (DRS) were performed using a Shimadzu UV-2101 PC spectrophotometer in the range of 200–800 nm. The photoluminescence (PL) spectra were recorded by using a Hitachi F-4500 spectrometer. The actual contents of Cu, Zn and Ag in the catalysts were detected by an inductively coupled plasma emission spectrometer (ICP).

2.4 Photocatalytic reaction procedure

To measure the photocatalytic activity of the obtained samples, the photodegradation of RhB aqueous solutions were performed under visible-light irradiation using a 300 W xenon lamp with a UV cut-off filter (the output spectrum of 320–780

nm). 20 mg of the $Ag/Cu_{0.25}Zn_{0.75}S$ samples were dispersed into 50 mL of 50 mg L^{-1} RhB solution. The suspensions were stirred for 1 h in the dark prior to irradiation to achieve the absorption–desorption equilibrium. 5 mL of the samples were taken out every 10 min and centrifuged for analysis using UV-vis spectroscopy (Unico UV-4802) during illumination. The impact of solution pH and hydrogen peroxide on the photodegradation of RhB were investigated. The stability of $Ag/Cu_{0.25}Zn_{0.75}S$ with optimal performance was performed for five cycles according to the above reaction conditions. The used $11-Ag/Cu_{0.25}Zn_{0.75}S$ sample was washed with deionized water and ethanol and vacuum-dried at 60 °C for 6 h; it was then reused for the photodegradation of RhB. Moreover, the degradation efficiency of MV and CIP by $11-Ag/Cu_{0.25}Zn_{0.75}S$ with an optimal performance was compared with that of RhB under the same conditions. In addition, the active species (superoxide radical ($\cdot O_2^{-}$), hydroxyl radical ($\cdot OH$) and hole (h^{+})) were evaluated by adding to the free radical captures (p-BQ, t-BuOH, and EDTA-2Na), respectively.
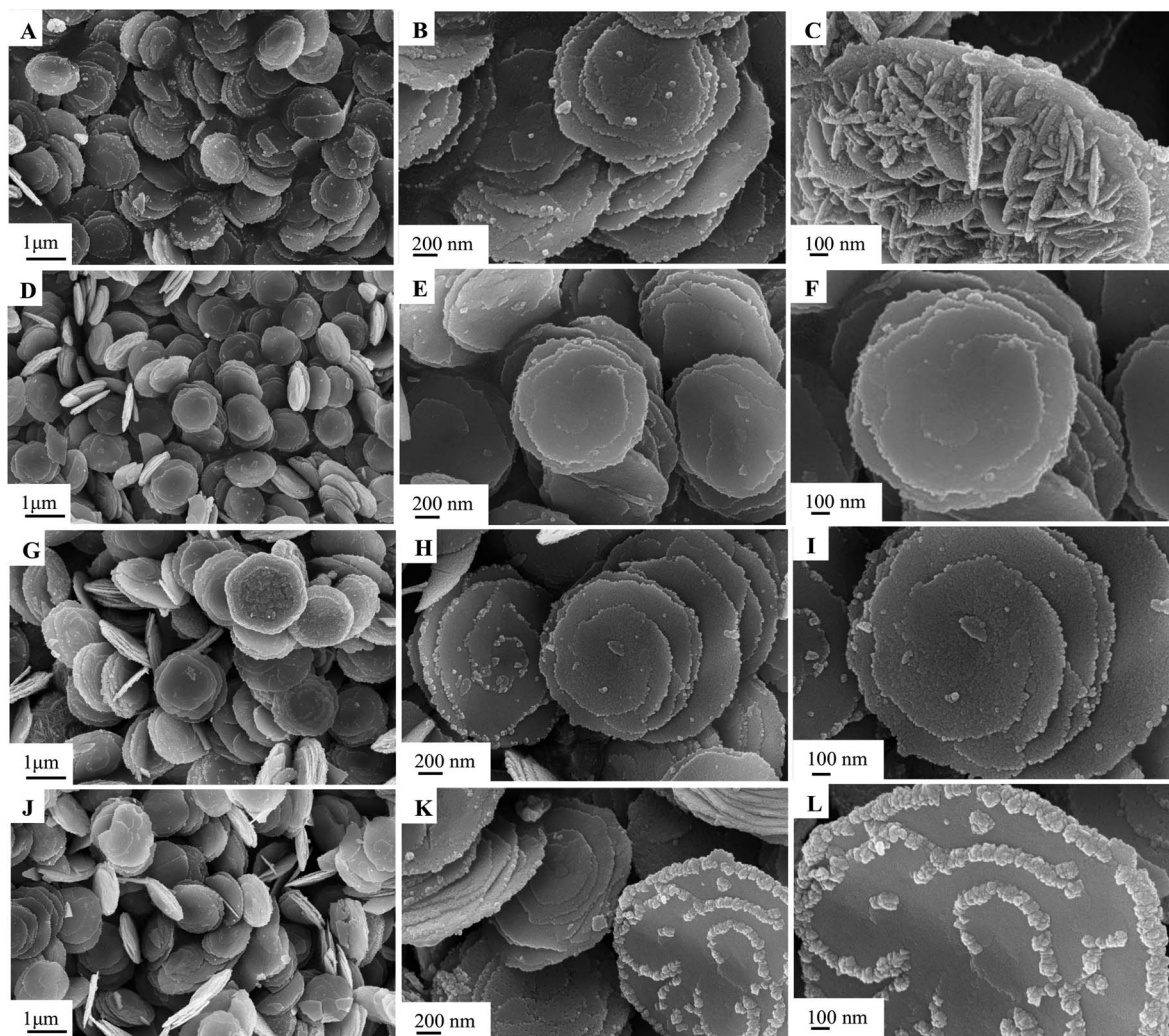
Fig. 3   SEM images of $Cu_{0.25}Zn_{0.75}S$ prepared with varying Cu and Zn total contents of 2 mmol (A–C), 4 mmol (D–F), 6 mmol (G–I), 8 mmol (J–L).

3.   Results and discussion

3.1   Characterization of the photocatalysts

The morphology and structure of the as-synthesized samples in different conditions were characterized by SEM, as shown in Fig. 1–3. The obtained $Cu_{0.25}Zn_{0.75}S$ samples were uniform nanodisks. Temperature had a slight influence on the shape and structure of the products (Fig. 1). The crystallinity of the products increased with temperature (Fig. 1). Therefore, the reaction temperature in subsequent experiments was 200 °C. Upon further prolonging the reaction time, the diameter of the nanodisk increased, and extra crystal particles were deposited on the nanodisks (Fig. 2). The optimal reaction time was 6 h. The concentrations of Cu^{2+} and Zn^{2+} also influenced the
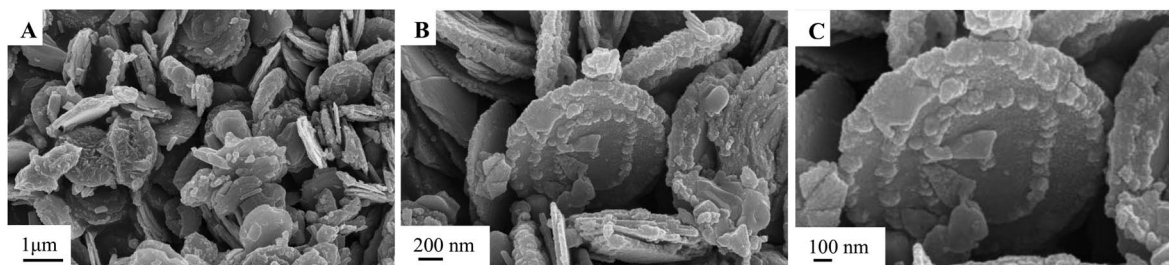

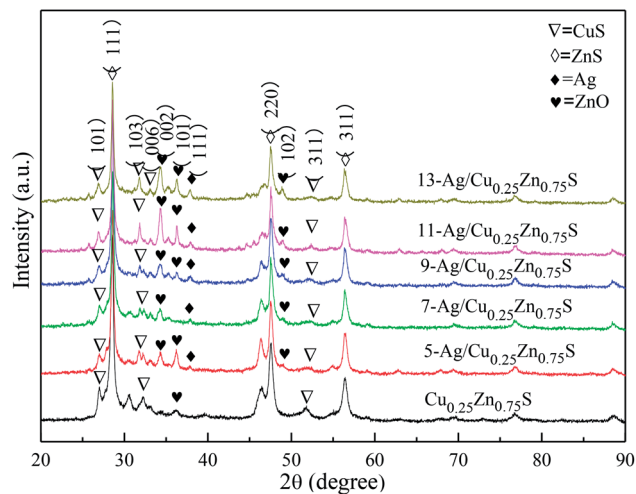Fig. 4   SEM images of 11-Ag/$Cu_{0.25}Zn_{0.75}S$.

Fig. 5 XRD patterns of Ag/Cu$_{0.25}$Zn$_{0.75}$S and Cu$_{0.25}$Zn$_{0.75}$S.

morphology and scale of the nanodisks. At low concentrations, the formed CuS and ZnS nanoparticles were limited, which resulted in the incomplete growth of the Cu$_{0.25}$Zn$_{0.75}$S nanodisks (Fig. 3A–C). When the total mass of cupric nitrate and zinc nitrate was 4 mmol, the CuS and ZnS nanoparticles grew in an orientation to form perfect nanodisks (Fig. 3D–F). However, as the amount of Cu^{2+} and Zn^{2+} continued to increase, the excess nanoparticles were deposited onto the surface of the nanodisks (Fig. 3G–L). Thus, the optimal amount of Cu^{2+} and Zn^{2+} was 4 mmol. As shown in Fig. 4, the SEM results suggested that the

Ag nanoparticles were dispersed on the surface of the Cu$_{0.25}$Zn$_{0.75}$S nanodisks.

The XRD patterns of the as-obtained Cu$_{0.25}$Zn$_{0.75}$S and Ag/Cu$_{0.25}$Zn$_{0.75}$S samples loaded with 5–13% silver are shown in Fig. 5. The Cu$_{0.25}$Zn$_{0.75}$S composite consisted of CuS and ZnS crystals and a small amount of ZnO. The actual contents of Cu and Zn in Cu$_{0.25}$Zn$_{0.75}$S detected by ICP showed that the content of Cu and Zn was similar, and their content accounted for about 70 wt% of Cu$_{0.25}$Zn$_{0.75}$S (Table 2). This result also implied the existence of zinc oxide. The peaks at $2\theta = 38.1°$ and $64.4°$ were indexed to the (111) and (220) planes of Ag with a cubic structure, and the intensity of the peaks was enhanced with increasing Ag amount. At low Ag content, the diffraction peaks of Ag were not apparent. The mapping images also indicated that Ag, Cu, Zn and S elements were observed in the Ag-loaded Cu$_{0.25}$Zn$_{0.75}$S samples (Fig. 6). The actual content of Ag loading was 7.48 wt% (Table 2). It is worth noting that the characteristic peak of ZnO was more obvious after loading Ag, especially in the 11-Ag/Cu$_{0.25}$Zn$_{0.75}$S sample. This suggests that the loading of Ag promotes the formation of ZnO. The reason may be that oxygen generated during the decomposition of silver nitrate contributes to the formation of ZnO. The actual contents of Cu and Zn in 11-Ag/Cu$_{0.25}$Zn$_{0.75}$S also showed that though the contents of Cu and Zn slightly decreased, the proportion in Cu$_{0.25}$Zn$_{0.75}$S increased. This also implied that part of the ZnS may be converted into ZnO.

Fig. 7 showed that the various Ag amounts of Ag/Cu$_{0.25}$Zn$_{0.75}$S catalysts displayed the type II hysteresis loop of the nitrogen adsorption–desorption curve. The BET surface
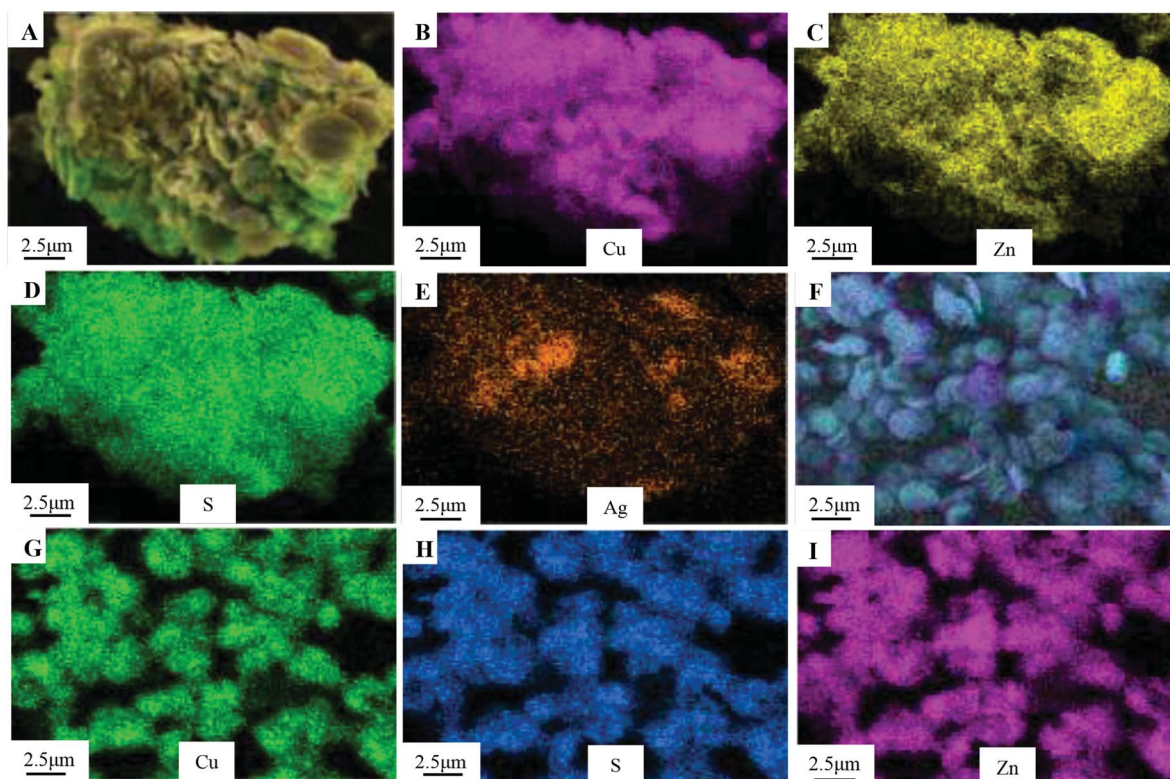

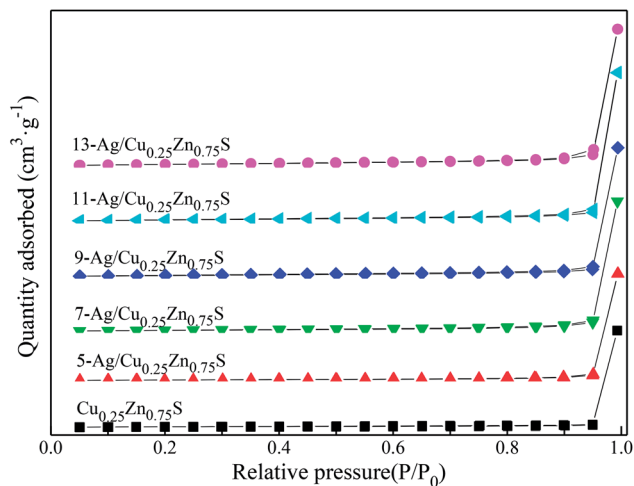Fig. 6 Element mapping images of 11-Ag/Cu$_{0.25}$Zn$_{0.75}$S (A–E) and Cu$_{0.25}$Zn$_{0.75}$S (F–I).

Fig. 7 N_2 adsorption–desorption isotherms of $Ag/Cu_{0.25}Zn_{0.75}S$ and $Cu_{0.25}Zn_{0.75}S$.

Table 1 Texture parameters of $Cu_{0.25}Zn_{0.75}S$ and $Ag/Cu_{0.25}Zn_{0.75}S$

Samples	Specific surface area ($m^2\ g^{-1}$)	Pore size (nm)	Pore volume ($cm^3\ g^{-1}$)	Band gap energy[a] (eV)
$Cu_{0.25}Zn_{0.75}S$	35.26	1.54	0.082	2.25
5-$Cu_{0.25}Zn_{0.75}S$	31.34	1.47	0.071	1.93
7-$Cu_{0.25}Zn_{0.75}S$	29.67	1.34	0.064	1.79
9-$Cu_{0.25}Zn_{0.75}S$	27.32	1.44	0.059	1.75
11-$Cu_{0.25}Zn_{0.75}S$	25.49	1.35	0.053	1.69
13-$Cu_{0.25}Zn_{0.75}S$	24.32	1.31	0.051	1.83

[a] The band gap energy of the $Cu_{0.25}Zn_{0.75}S$ and $Ag/Cu_{0.25}Zn_{0.75}S$ samples were calculated using the Kubelka–Munk equation.

areas of the $Ag/Cu_{0.25}Zn_{0.75}S$ catalysts decreased with the increase in the Ag amount (Table 1). Fig. 8 showed the UV-visible absorption spectra of the $Cu_{0.25}Zn_{0.75}S$ and $Ag/Cu_{0.25}Zn_{0.75}S$ composites. In the UV-visible absorption spectra of $Cu_{0.25}Zn_{0.75}S$, a significant increase in the absorption at wavelengths shorter than 350 nm can be assigned to the intrinsic band-gap absorption of ZnS.[5,38,39] The absorption between 500 nm and 800 nm can be attributed to the d–d transition of Cu^{2+}, displaying the substitution of Zn^{2+} to form CuS.[4] The loading of Ag enhanced the absorption of visible light. All $Ag/Cu_{0.25}Zn_{0.75}S$ samples had a wide adsorption range from 250 to 800 nm, with especially strong absorption in the range of 700–800 nm, implying that these samples had good visible-light photocatalytic activity. The band gap energy values of all the

Table 2 The actual contents of Cu, Zn and Ag in the $Cu_{0.25}Zn_{0.75}S$ and 11% $Ag/Cu_{0.25}Zn_{0.75}S$ samples detected by ICP

sample	Cu	Zn	Ag
$Cu_{0.25}Zn_{0.75}S$	32.31%	37.86%	
11% $Ag/Cu_{0.25}Zn_{0.75}S$	31.44%	35.90%	7.48%

samples were calculated using the Kubelka–Munk equation (Table 1). The estimated band gap energy value for 11-$Ag/Cu_{0.25}Zn_{0.75}S$ was the lowest, which was 1.69 eV. This means that 11-$Ag/Cu_{0.25}Zn_{0.75}S$ can more efficiently utilize visible light to drive photochemical reactions.[6,40]

XPS was used to illuminate the surface composition and electronic state of $Cu_{0.25}Zn_{0.75}S$ and 11-$Ag/Cu_{0.25}Zn_{0.75}S$ samples. Fig. 9C and F showed that the two typical binding energy peaks of Zn 2p at 1020.9 8 eV and 1043.98 eV were ascribed to the binding energies of Zn $2p_{3/2}$ and Zn $2p_{1/2}$, respectively, indicating the presence of pure Zn^{2+} ions.[7] The binding energy peaks of Cu $2p_{3/2}$ and Cu $2p_{1/2}$ at 931.48 eV and 951.08 eV corresponded to the typical values of Cu^{2+} in CuS (Fig. 9B and H).[41] Fig. 9D and I showed that the peaks at 160.99 eV and 162.28 eV were attributed to S $2p_{3/2}$ and S $2p_{1/2}$, respectively, matching well with that of S^{2-} ions.[42–45] The characteristic binding energies of Ag $3d_{5/2}$ and $3d_{3/2}$ were 367.38 eV and 373.28 eV (Fig. 9A), respectively, implying the existence of zero valent Ag.[46–48] These results indicated that the surface of 11-$Ag/Cu_{0.25}Zn_{0.75}S$ sample mainly contained Zn^{2+}, Cu^{2+}, Ag and S^{2-}.

3.2 Photocatalytic capacity

$Ag/Cu_{0.25}Zn_{0.75}S$ was performed for the degradation of organic contaminants under visible-light irradiation, such as RhB, MV and CIP. In contrast with $Cu_{0.25}Zn_{0.75}S$, loading Ag could improve the photocatalytic activity of $Cu_{0.25}Zn_{0.75}S$ due to its surface plasmon resonance effect. The photodegradation efficiency of RhB increased first and then decreased with the increase in the Ag loading content, of which 11-$Ag/Cu_{0.25}Zn_{0.75}S$ exhibited the best photocatalyst activity for the removal of RhB (Fig. 10A). Ag nanoparticles, serving as the electron sink, were responsible for the efficient separation of photoexcited electron–hole pairs. However, high Ag content led to the overlapping agglomerates and reduced surface area.[29] This negative effect was unsuitable for visible-light-driven photocatalytic performance. 11-$Ag/Cu_{0.25}Zn_{0.75}S$ had better photocatalytic activity and efficiency compared with some similar catalysts, such as Cu_2ZnSnS_4–Pt and Cu_2ZnSnS_4–Au heterostructured nanoparticles,[39] CuS/ZnS core/shell nanocrystals,[18] $Zn_{1-x}Cu_xS$ and $Zn_{1-x}Ni_xS$ nanoparticles,[14] Ce_2S_3–ZnS–CuS nanoparticles,[28] graphene oxide/Ag/Ag_2S–TiO_2 nanocomposites[36] and ZnS–Ag_2S ternary composites.[7]

pH plays an important role in the photocatalytic reactions for the removal of the pollutants.[49] 11-$Ag/Cu_{0.25}Zn_{0.75}S$ had higher photocatalytic activity under acidic conditions (pH = 4.17) due to the modified surface charge of the photocatalyst and the maximized active radicals (Fig. 10B). The optimized pH condition may be suitable for the formation of ·OH and ·O_2^- radicals with the consumed e^-/h^+ pairs, inducing the promising photocatalytic reaction. In the photocatalytic system, ·O_2^- radicals generated from O_2 molecules can react with H^+ ions to form the ·OOH species, which were further reduced to H_2O_2 molecules. Subsequently, H_2O_2 can react with an e^- to generate OH^- ions and ·OH radicals, of which OH^- ions are consumed by h^+ to generate ·OH radicals. As the electron acceptor,
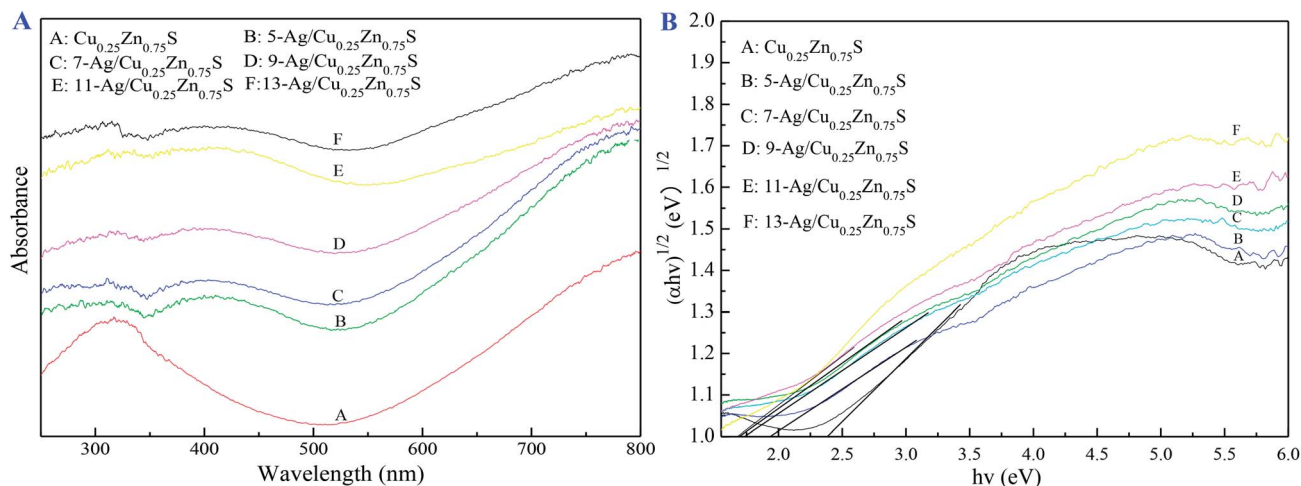
Fig. 8 UV-vis spectra of $Cu_{0.25}Zn_{0.75}S$ and $Ag/Cu_{0.25}Zn_{0.75}S$.
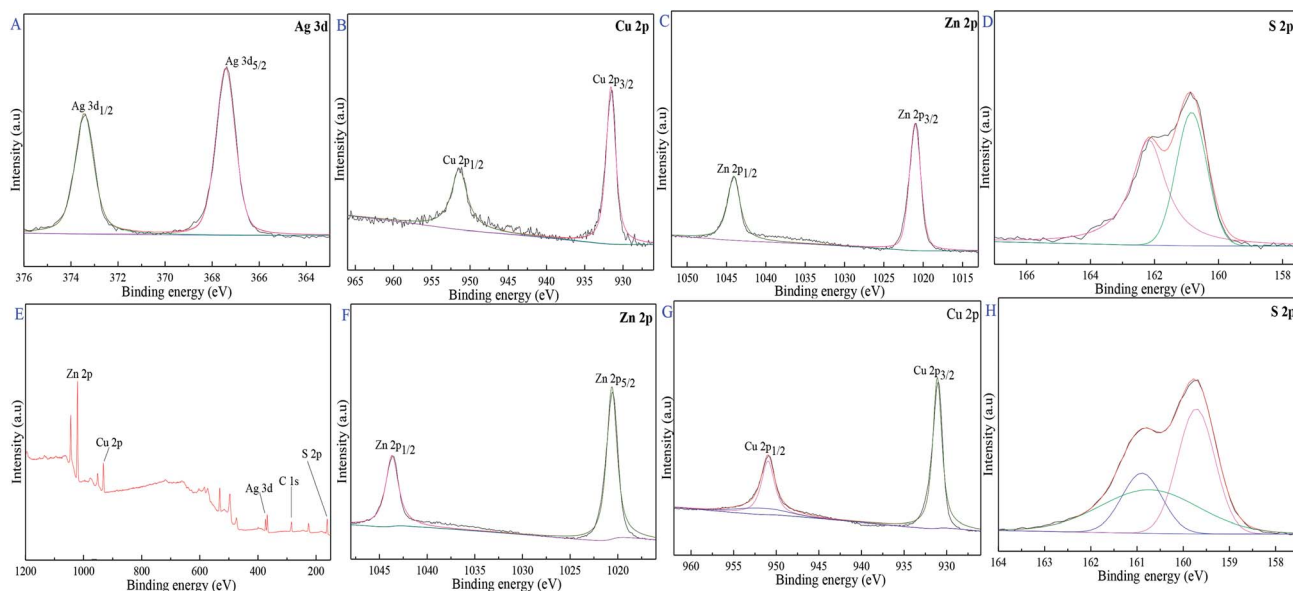
Fig. 9 XPS spectra of $11\text{-}Ag/Cu_{0.25}Zn_{0.75}S$ and $Cu_{0.25}Zn_{0.75}S$, $11\text{-}Ag/Cu_{0.25}Zn_{0.75}S$ (A–E), $Cu_{0.25}Zn_{0.75}S$ (F–H).

moderate amounts of H_2O_2 promote the separation of electrons and holes and produces ·OH radicals. As shown in Fig. 10C and D, the best photodegradation activity for RhB removal was obtained by the presence of 100 μL of H_2O_2. The photocatalytic activity of $11\text{-}Ag/Cu_{0.25}Zn_{0.75}S$ increased first and then decreased with an increase in the H_2O_2 content due to the viable ·OH radicals scavenged by excess H_2O_2.[50] The durability of $11\text{-}Ag/Cu_{0.25}Zn_{0.75}S$ for the visible-light-driven photocatalytic degradation of RhB changed little after five cycles, as shown in Fig. 10E. The morphology and structure of the used $11\text{-}Ag/Cu_{0.25}Zn_{0.75}S$ sample were not influenced during the cycle testing experiment (Fig. 11), indicating the superior stability of $11\text{-}Ag/Cu_{0.25}Zn_{0.75}S$.

To further investigate the photodegradation activity of $11\text{-}Ag/Cu_{0.25}Zn_{0.75}S$ on organic pollutants, MV and CIP were also carried out under the same conditions. As shown in Fig. 10F, MV was completely removed within 30 min, and the degradation efficiency of CIP was about 80% after 60 min under visible-light irradiation. It was concluded that $11\text{-}Ag/Cu_{0.25}Zn_{0.75}S$ was a potential photocatalyst for the removal of organic pollutants.

The trapping experiments were conducted to investigate the active radicals in the photocatalytic process of RhB removal, of which ethylenediamine tetraacetic acid disodium salt (EDTA-2Na), *p*-benzoquinone (*p*-BQ) and *tert*-butanol (*t*-BuOH) served as the trapping agents for h^+, $·O_2^-$ and ·OH radicals, respectively.[8,51–53] As shown in Fig. 12A, EDTA-2Na slightly suppressed the photodegradation activity, implying that the h^+ radical was not crucial in the photocatalysis process. In contrast, only about 40% of RhB was decomposed by $11\text{-}Ag/Cu_{0.25}Zn_{0.75}S$ after 60 min in the presence of *p*-BQ. It was suggested that the $·O_2^-$
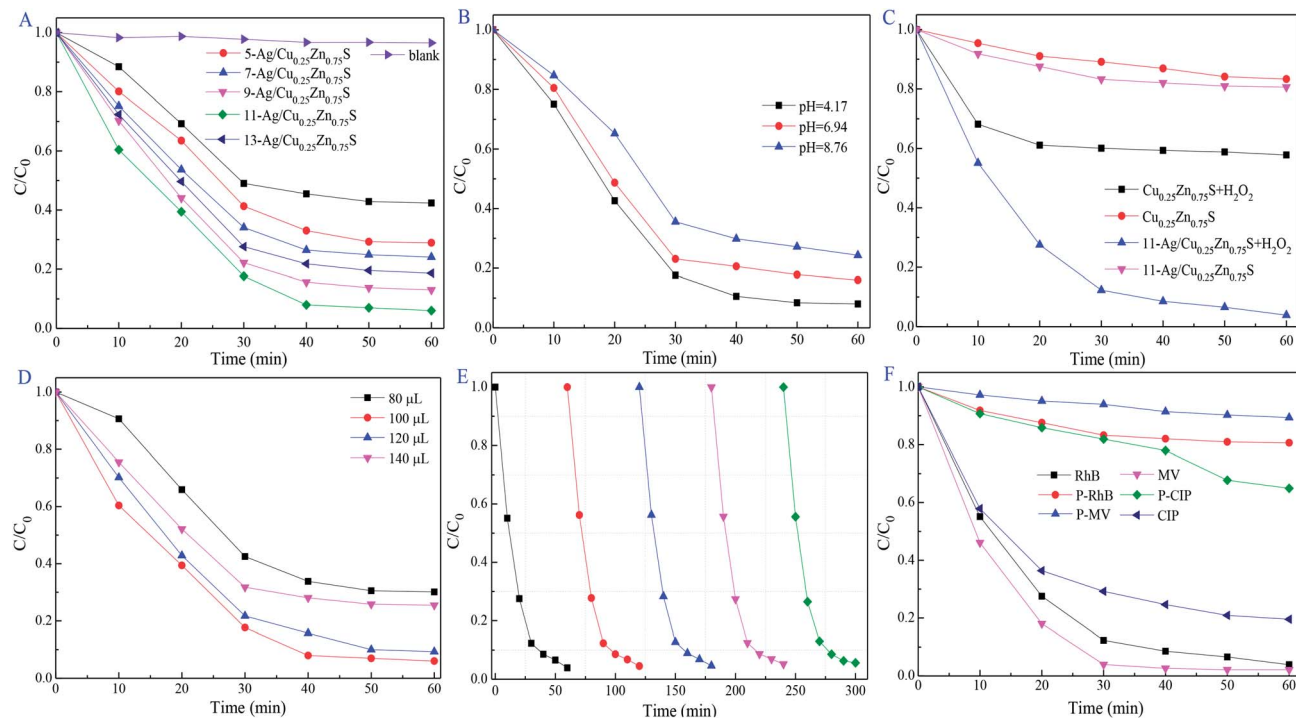
Fig. 10 Influence of Ag loading concentration in Ag/Cu$_{0.25}$Zn$_{0.75}$S samples (A), pH value (B), effects of H$_2$O$_2$ dosage (C and D), the cycling degradation (E) and different organic matter (F) on photodegradation activity.
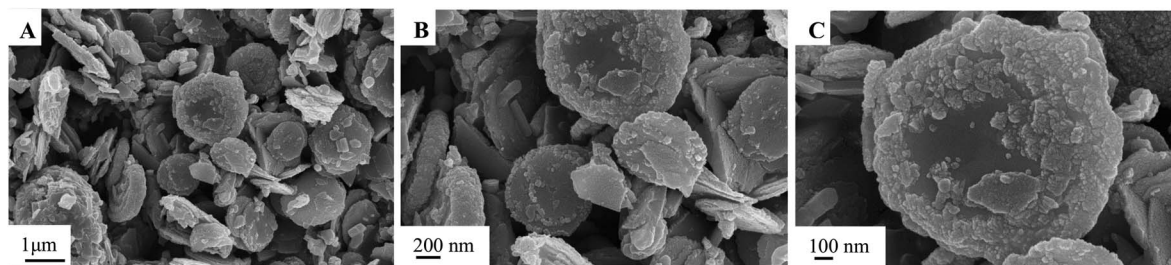

Fig. 11 SEM images of 11-Ag/Cu$_{0.25}$Zn$_{0.75}$S after the photodegradation reaction.
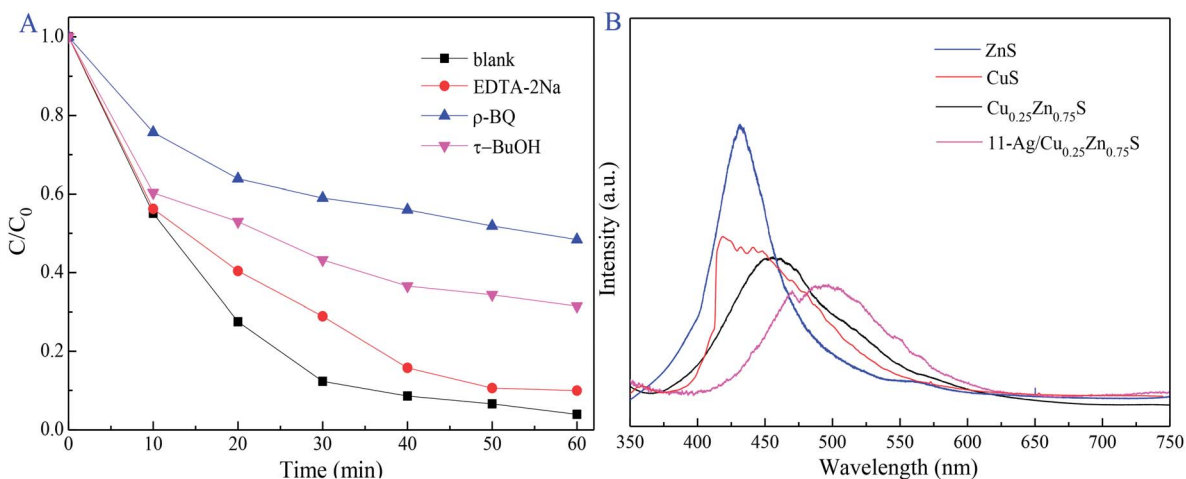

Fig. 12 Influence of the radical scavenger on photodegradation activity and PL spectra (A) of ZnS, CuS, Cu$_{0.25}$Zn$_{0.75}$S and (B) 11-Ag/Cu$_{0.25}$Zn$_{0.75}$S.

radical is the dominant oxidative species. The reduced degradation rate was also detected by the addition of *t*-BuOH, signifying the important role of the ·OH radical.

PL emission spectrum was widely used for illustrating the photo-generated electron–hole pair recombination process.[54] Compared with CuS, ZnS and $Cu_{0.25}Zn_{0.75}S$, 11-Ag/$Cu_{0.25}Zn_{0.75}S$ exhibited a lower photoluminescence intensity at room temperature (Fig. 12B). It was concluded that the low recombination of photoexcited electron–hole pairs led to the superior photocatalytic activity of 11-Ag/$Cu_{0.25}Zn_{0.75}S$.

4.   Conclusion

$Cu_{0.25}Zn_{0.75}S$ and Ag/$Cu_{0.25}Zn_{0.75}S$ photocatalysts were prepared by the hydrothermal method and the photocatalytic deposition method, respectively. Ag loading enhanced the photocatalytic activity of the $Cu_{0.25}Zn_{0.75}S$ nanodisks, and the optimal amount of Ag loading was 11 wt% (the actual content of Ag loading was 7.48 wt%). 11-Ag/$Cu_{0.25}Zn_{0.75}S$ had great photocatalytic activity and stability for RhB, in addition to its excellent photodegradation effect on MV and CIP. $·O_2^-$ is mainly responsible for the efficient activity of the photocatalytic process. Ag loading can efficiently separate the photogenerated electrons and holes and promote the interfacial electron transfer processes to remarkably enhance the photocatalytic activity.

Conflicts of interest

There are no conflicts to declare.

Acknowledgements

References

1 J. Zhang, J. Yu, Y. Zhang, Q. Li and J. R. Gong, *Nano Lett.*, 2011, **11**, 4774–4779.

2 P. Wang, Y. Gao, P. Li, X. Zhang, H. Niu and Z. Zheng, *ACS Appl. Mater. Interfaces*, 2016, **8**, 15820–15827.

3 X. Xu, J. Bullock, L. T. Schelhas, E. Z. Stutz, J. J. Fonseca, M. Hettick, V. L. Pool, F. T. Kong, M. F. Toney and X. Fang, *Nano Lett.*, 2016, **16**, 1925–1932.

4 C. Feng, X. Meng, X. Song, X. Feng, Y. Zhao and G. Liu, *RSC Adv.*, 2016, **6**, 110266–110273.

5 Y. B. Shao, L. H. Wang and J. H. Huang, *RSC Adv.*, 2016, **6**, 84493–84499.

6 V. Selvaraj, *RSC Adv.*, 2016, **6**, 4227–4236.

7 D. A. Reddy, R. Ma, M. Y. Choi and T. K. Kim, *Appl. Surf. Sci.*, 2015, **324**, 725–735.

8 H. Wei, W. A. Mcmaster, J. Z. Y. Tan, L. Cao, D. Chen and R. A. Caruso, *J. Phys. Chem. C*, 2017, **121**, 22114–22122.

9 D. P. Leonard, H. Pan and M. D. Heagy, *ACS Appl. Mater. Interfaces*, 2015, **7**, 24543–24549.

10 M. Saranya, R. Ramachandran, E. J. J. Samuel, S. K. Jeong and A. N. Grace, *Powder Technol.*, 2015, **279**, 209–220.

11 M. Li, J. Su and L. Guo, *Int. J. Hydrogen Energy*, 2008, **33**, 2891–2896.

12 T. T. Thanhthuy, P. Sheng, C. A. Huang, J. Li, L. Chen, L. Yuan, C. A. Grimes and Q. Cai, *Chem. Eng. J.*, 2012, **210**, 425–431.

13 J. Kaur, M. Sharma and O. P. Pandey, *Superlattices Microstruct.*, 2015, **77**, 35–53.

14 H. R. Pouretedal and M. H. Keshavarz, *J. Alloys Compd.*, 2010, **501**, 130–135.

15 B. Zeng, X. Chen, C. Chen, X. Ning and W. Deng, *J. Alloys Compd.*, 2014, **582**, 774–779.

16 J. Yu, J. Zhang and S. Liu, *J. Phys. Chem. C*, 2010, **114**, 13642–13649.

17 S. Harish, J. Archana, M. Navaneethan, S. Ponnusamy, A. Singh, V. Gupta, D. K. Aswal, H. Ikeda and Y. Hayakawa, *RSC Adv.*, 2017, **7**, 34366–34375.

18 U. T. D. Thuy, N. Q. Liem, C. M. A. Parlett, G. M. Lalev and K. Wilson, *Catal. Commun.*, 2014, **44**, 62–67.

19 M. Feng, H. Zhou, W. Guo, D. Zhang, L. Ye, W. Li, J. Ma, G. Wang and S. Chen, *J. Alloys Compd.*, 2018, **750**, 750–756.

20 X. Xu, Q. Chen, H. Yuan, N. Yi, J. Chen, X. Zhu, Y. Yamaguchi and X. Dou, *J. Mater. Sci.: Mater. Electron.*, 2017, **28**, 18085–18089.

21 K. Yang and M. Ichimura, *Jpn. J. Appl. Phys.*, 2011, **50**, 584–587.

22 K. Yang, Y. Nakashima and M. Ichimura, *J. Electrochem. Soc.*, 2012, **159**, H250–H254.

23 A. Giaccherini, G. Montegrossi, F. D. Benedetto and M. Innocenti, *Electrochim. Acta*, 2018, **262**, 135–143.

24 B. Tong and M. Ichimura, *Jpn. J. Appl. Phys.*, 2016, **55**, 098004.

25 D. Man, K. Yang and M. Ichimura, *Semicond. Sci. Technol.*, 2012, **27**, 125007.

26 A. M. Diamond, L. Corbellini, K. R. Balasubramaniam, S. Chen, S. Wang, T. S. Matthews, L. W. Wang, R. Ramesh and J. W. Ager, *Phys. Status Solidi*, 2012, **209**, 2101–2107.

27 D. E. Ortíz-Ramos, L. A. González and R. Ramirez-Bon, *Mater. Lett.*, 2014, **124**, 267–270.

28 C. Shifu, J. Mingsong and Y. Yunguang, *J. Nanosci. Nanotechnol.*, 2012, **12**, 4898–4904.

29 C. Yu, J. C. Yu, C. Fan, H. Wen and S. Hu, *Mater. Sci. Eng., B*, 2010, **166**, 213–219.

30 L. Sun, S. Zhao, Z. Gao and Z. Cheng, *Chem. J. Chin. Univ.*, 2017, **38**, 907–914.

31 P. Rai, S. M. Majhi, Y. T. Yu and J. H. Lee, *RSC Adv.*, 2015, **5**, 76229–76248.

32 M. Kimi, L. Yuliati and M. Shamsuddin, *Adv. Mater. Res.*, 2014, **1024**, 368–371.

33 G. Murugadoss, R. Jayavel, M. R. Kumar and R. Thangamuthu, *Appl. Nanosci.*, 2016, **6**, 503–510.

34 J. Kaur, A. Gupta and O. P. Pandey, *Sol. Energy*, 2018, **176**, 678–687.

35 M. Mittal, A. Gupta and O. P. Pandey, *Sol. Energy*, 2018, **165**, 206–216.

36 S. Shuang, L. Ruitao, C. Xiaoyang, X. Zheng, Z. Jian and Z. Zhengjun, *RSC Adv.*, 2018, **8**, 5784–5791.

37 X. Zheng, W. Fu, H. Peng and J. Wen, *J. Environ. Chem. Eng.*, 2018, **6**, 9–18.

38 S. Zu, Z. Wang, B. Liu, X. Fan and G. Qian, *J. Alloys Compd.*, 2009, **476**, 689–692.

39 X. Yu, A. Shavel, X. An, Z. Luo, M. Ibánez and A. Cabot, *J. Am. Chem. Soc.*, 2014, **136**, 9236–9239.

40 L. Wang, B. Cao, K. Wei, M. Hybertsen, K. Maeda, K. Domen and P. G. Khalifah, *Inorg. Chem.*, 2013, **44**, 9192–9205.

41 C. Feng, L. Zhang, M. Yang, X. Song, H. Zhao, Z. Jia, K. Sun and G. Liu, *ACS Appl. Mater. Interfaces*, 2015, **7**, 15726.

42 X. J. Zhang, G. S. Wang, Y. Z. Wei, L. Guo and M. S. Cao, *J. Mater. Chem. A*, 2013, **1**, 12115–12122.

43 D. A. Reddy, D. H. Kim, S. J. Rhee, C. U. Jung, B. W. Lee and C. Liu, *J. Alloys Compd.*, 2014, **588**, 596–604.

44 C. Chen, Y. Xie, G. Ali, S. H. Yoo and S. O. Cho, *Nanoscale Res. Lett.*, 2011, **6**, 462.

45 W. Zhang, L. Zhang, Z. Hui, X. Zhang and Y. Qian, *Solid State Ionics*, 2000, **130**, 111–114.

46 H. Yu, H. Yang, R. Yao and X. Z. Guo, *Acta Phys.-Chim. Sin.*, 2014, **30**, 1384–1390.

47 H. Yang, Y. Liu, Q. Shen, L. Chen, W. You, X. Wang and J. Sheng, *J. Mater. Chem.*, 2012, **22**, 24132–24138.

48 K. Nischala, T. N. Rao and N. Hebalkar, *Colloids Surf., B*, 2011, **82**, 203–208.

49 M. López-Muñoz, J. Aguado, A. Arencibia and R. Pascual, *Appl. Catal., B*, 2011, **104**, 220–228.

50 L. Wei, C. Shifu, Z. Wei and Z. Sujuan, *J. Hazard. Mater.*, 2009, **164**, 154.

51 L. Yin, Y. Shi, L. Lu, R. Fang, X. Wan and H. Shi, *Catalysts*, 2016, **6**, 69.

52 Z. Chen, W. Wang, Z. Zhang and X. Fang, *J. Phys. Chem. C*, 2013, **117**, 19346–19352.

53 F. T. Li, X. J. Wang, Y. Zhao, J. X. Liu, Y. J. Hao, R. H. Liu and D. S. Zhao, *Appl. Catal., B*, 2014, **144**, 442–453.

54 H. Yamashita, A. Yuichi Ichihashi, M. Anpo, M. Hashimoto, C. Louis and M. Che, *ChemInform*, 1997, **28**, 16041–16044.